Monthly Notices
of the
ROYAL ASTRONOMICAL SOCIETY

MNRAS **520,** 3368–3382 (2023) https://doi.org/10.1093/mnras/stad281
Advance Access publication 2023 January 27

Thermal and reionization history within a large-volume semi-analytic galaxy formation simulation

Sreedhar Balu,[1,2★] Bradley Greig,[1,2] Yisheng Qiu,[3] Chris Power,[2,4] Yuxiang Qin,[1,2] Simon Mutch[1,2] and J. Stuart B. Wyithe[1,2]

[1] *School of Physics, University of Melbourne, Parkville, VIC 3010, Australia*
[2] *ARC Centre of Excellence for All Sky Astrophysics in 3 Dimensions (ASTRO 3D)*
[3] *Institute for Astronomy, School of Physics, Zhejiang University, Hangzhou 310027, China*
[4] *International Centre for Radio Astronomy Research, M468, University of Western Australia, 35 Stirling Hwy, Perth, WA 6009, Australia*

Accepted 2023 January 23. Received 2022 December 19; in original form 2022 October 18

ABSTRACT

We predict the 21-cm global signal and power spectra during the Epoch of Reionization using the MERAXES semi-analytic galaxy formation and reionization model, updated to include X-ray heating and thermal evolution of the intergalactic medium. Studying the formation and evolution of galaxies together with the reionization of cosmic hydrogen using semi-analytic models (such as MERAXES) requires N-body simulations within large volumes and high-mass resolutions. For this, we use a simulation of side-length $210\,h^{-1}$ Mpc with 4320^3 particles resolving dark matter haloes to masses of $5\times10^8\,h^{-1}\,\mathrm{M}_\odot$. To reach the mass resolution of atomically cooled galaxies, thought to be the dominant population contributing to reionization, at $z=20$ of $\sim2\times10^7\,h^{-1}\,\mathrm{M}_\odot$, we augment this simulation using the DARKFOREST Monte Carlo merger tree algorithm (achieving an effective particle count of $\sim10^{12}$). Using this augmented simulation, we explore the impact of mass resolution on the predicted reionization history as well as the impact of X-ray heating on the 21-cm global signal and the 21-cm power spectra. We also explore the cosmic variance of 21-cm statistics within $70^3\,h^{-3}\,\mathrm{Mpc}^3$ sub-volumes. We find that the midpoint of reionization varies by $\Delta z\sim0.8$ and that the cosmic variance on the power spectrum is underestimated by a factor of 2–4 at $k\sim0.1$–$0.4\,\mathrm{Mpc}^{-1}$ due to the non-Gaussian nature of the 21-cm signal. To our knowledge, this work represents the first model of both reionization and galaxy formation which resolves low-mass atomically cooled galaxies while simultaneously sampling sufficiently large scales necessary for exploring the effects of X-rays in the early Universe.

Key words: galaxies: evolution – galaxies: high redshift – dark ages, reionization, first stars.

1 INTRODUCTION

The formation of the first luminous objects during the cosmic dawn resulted in the ionization of the cosmic H I gas, rendering the intergalactic medium (IGM) transparent to UV photons. This period, termed the Epoch of Reionization (EoR), constitutes the last major phase change of hydrogen in the Universe and had an impact on subsequent galaxy formation and evolution (Barkana & Loeb 2001). A promising probe of this period is the 21-cm hyperfine spin-flip transition of H I which is sensitive to the evolution of the thermal and ionization states of the IGM (Furlanetto, Peng Oh & Briggs 2006b).

A number of low-frequency radio telescope arrays are in operation or are planned to detect this signal. Current instruments (MWA,[1] LOFAR,[2] HERA[3]) aim to detect the signal statistically via the 21-cm power spectrum (21-cm PS; Morales & Wyithe 2010). While a detection has not yet been made, in recent years there has been significant progress in lowering the available upper limits (Mertens et al. 2020; Trott et al. 2020; The HERA Collaboration et al. 2022). In addition, the evolution of the all-sky averaged 21-cm global signal (21-cm GS) is being sought with experiments such as EDGES (Bowman et al. 2018) and SARAS (Singh et al. 2022). In the near future, the Square Kilometre Array (SKA; Koopmans et al. 2014)[4] will provide an unprecedented ability to place observational constraints on the physics of this era by enabling the production of detailed 3D 21-cm maps showing the distribution and evolution of the cosmic H I.

For interpreting current and future observations, it is important that realistic simulations of the early Universe are available and many authors have contributed to this effort (see Gnedin & Madau 2022 for a recent review). Simulations of the EoR are made challenging by the large range of scales involved. The main drivers controlling the ionization and thermal states of the H I are respectively the intense UV and X-ray photons from star-forming galaxies (see Mesinger 2019 and references therein). X-ray photons have mean-free paths of the order of 10–100s of Mpc in the high-z Universe, while the

---

★ E-mail: bsreedhar@student.unimelb.edu.au

[1] www.mwatelescope.org

[2] www.astron.nl/telescopes/lofar

[3] reionization.org/

[4] www.skao.int

typical individual H II bubble sizes are ∼10–15 Mpc (Wyithe & Loeb 2004; Furlanetto, McQuinn & Hernquist 2006a). It has also been shown that simulation volumes of sidelength $\gtrsim 100\,h^{-1}$ Mpc are needed for convergent reionization histories (Iliev et al. 2014) while $\gtrsim 200\,h^{-1}$ Mpc are needed for convergent 21-cm PS (Kim et al. 2016; Kaur, Gillet & Mesinger 2020). These considerations necessitate simulations capable of resolving structures from a few Mpc in volumes of $\gtrsim$100 s Mpc on a side.

At the same time, realistic EoR modelling requires the ability to resolve haloes down to at least the hydrogen cooling limit corresponding to a halo virial temperature of $T_{\rm vir} \sim 10^4$K and virial mass (Barkana & Loeb 2001)

$$M_{\rm vir}(z) \sim 4.4 \times 10^3 \left(\frac{T_{\rm vir}}{1+z}\right)^{3/2} h^{-1}\,{\rm M}_{\odot}. \qquad (1)$$

These so-called atomically cooled haloes provide sites where gas efficiently cools via atomic line transitions to form stars. Thus, to realistically simulate a representative volume of the early Universe, one requires large simulation volumes as well as sufficiently high-mass resolutions.

Several techniques have been developed to simulate the EoR (Gnedin & Madau 2022). Seminumerical simulations (e.g. Santos et al. 2010; Mesinger, Furlanetto & Cen 2011; Maity & Choudhury 2022) typically associate ionizing photon sources with the density peaks of evolved Gaussian random fields. As these models do not require running computationally expensive *N*-body simulations, they are able to achieve very large volumes (Greig et al. 2022b) as well as efficiently explore the available parameter space (e.g. Greig & Mesinger 2015). Their main drawback is the absence of detailed physics which self-consistently models a realistic galaxy population. On the other hand, achieving high resolution in large-volume hydrodynamical simulations is computationally expensive (see for example Gnedin 2014; Ocvirk et al. 2016; Rosdahl et al. 2018; Kannan et al. 2022). However, the computational overhead associated with hydrodynamical simulations precludes their use in parameter exploration.

Semi-analytic models (SAMs; see Somerville & Davé 2015 for a review) of galaxy formation (e.g. Cole et al. 2002, Benson 2012, Croton et al. 2016, Cora et al. 2018, Lagos et al. 2018) typically take merger trees from comparatively cheaper dark matter-only *N*-body simulations and evolve key baryonic components which describe the physical processes involved in galaxy formation, growth, and evolution using simple but physically motivated prescriptions. Importantly, being based on *N*-body trees, the galaxies retain their association with the large-scale structure. These galaxy SAMs then provide a realistic galaxy population at a fraction of the cost of full hydrodynamical simulations. Coupling a galaxy SAM with a seminumerical reionization code can provide the best of both worlds: large-volume simulations of reionization with a self-consistent realistic population of galaxies. In this work, we use MERAXES (Mutch et al. 2016), developed as part of the DRAGONS (Dark-ages Reionization And Galaxy formation Observables from Numerical Simulations) program, which couples a galaxy SAM model designed for galaxies in the high-*z* Universe during the EoR with the seminumerical code 21CMFAST for simulating the reionization process.[5] Additionally, for the first time, we implement the evolution of the neutral hydrogen gas spin temperature into MERAXES, taking into account heating by X-ray photons.

We run our updated MERAXES on a new dark matter-only *N*-body simulation which has a volume of $210^3\,h^{-3}\,{\rm Mpc}^3$ with 4320^3 particles. This is the largest volume on which MERAXES has been deployed (previously $67.8^3\,h^{-3}\,{\rm Mpc}^3$; Qiu et al. 2019). To achieve sufficient mass resolution (atomic cooling limit at $z = 20$ of $\sim 2 \times 10^7\,h^{-1}\,{\rm M}_{\odot}$) within our simulations, we use DARKFOREST – a Monte Carlo algorithm-based code introduced in Qiu et al. (2020). This provides a unique data set modelling both individual galaxy formation and evolution during reionization in volumes large enough for exploring the effects of X-rays on the 21-cm signal from the cosmic dawn and the EoR. Importantly, this is the first time such a large volume coupled reionization and galaxy SAM has been performed to study the 21-cm signal into the cosmic dawn. With our large volume, we are able to explore the impact of cosmic variance across the 21-cm statistics.

The paper is organized as follows: Section 2 introduces the *N*-body simulations utilized in this work as well as its augmentation; Section 3 provides a brief summary of the MERAXES SAM and the calibration of its input model parameters. We analyse the resultant 21-cm signal from this model in Section 4 and explore the cosmic variance across a broad range of statistics in Section 5, and conclude in Section 6. Our simulations use the best-fitting parameters from the Planck Collaboration (2016): $h = 0.6751$, $\Omega_{\rm m} = 0.3121$, $\Omega_{\rm b} = 0.0490$, $\Omega_\Lambda = 0.6879$, $\sigma_8 = 0.8150$, and $n_s = 0.9653$. All quantities quoted are in comoving units unless otherwise stated.

2 *N*-BODY SIMULATIONS AND THEIR AUGMENTATION

In this section, we introduce the *N*-body simulation used in this work as well as an outline of the augmentation pipeline.

2.1 L210 simulation

We use the L210_N4320 (hereafter, L210) box of the GENESIS suite of *N*-body simulations (Power et al. in preparation). This simulation is $210\,h^{-1}$ Mpc on a side and consists of 4320^3 dark matter particles of mass $m_{\rm p} = 9.95 \times 10^6\,h^{-1}\,{\rm M}_{\odot}$. The halo mass resolution is $\sim 5 \times 10^8\,h^{-1}\,{\rm M}_{\odot}$ based on a minimum of 50 particles. The simulation was evolved from $z = 99$ down to $z = 5$ using the SWIFT code (Schaller et al. 2018) and the haloes were identified via friends-of-friends by the VELOCIRAPTOR halo-finder (Elahi et al. 2019a). Halo catalogues are saved over 120 snapshots evenly distributed in dynamical time between redshifts 30 and 5. The merger trees were generated using TREEFROG (Elahi et al. 2019b).

2.2 L210_AUG simulation

To increase the mass resolution of the L210 simulation from $\sim 5 \times 10^8\,h^{-1}\,{\rm M}_{\odot}$ to the atomic hydrogen cooling limit at $z = 20$ ($\sim 2 \times 10^7\,h^{-1}\,{\rm M}_{\odot}$), we augment it by extending the merger trees to lower mass haloes. This is achieved using DARKFOREST (Qiu et al. 2020), a Monte Carlo (MC) based algorithm which we summarize below. We call this new simulation L210_AUG, which provides a unique data set for exploring galaxy formation physics and its impact on the timing and morphology of the EoR. Fig. 1 shows the mass resolution of both L210_AUG (orange dashed) and L210 (blue dashed) along with the atomic cooling limit (dark grey curve) for the relevant redshifts. We point out that the augmentation algorithm works backward in time (in our case from $z = 5$).

---

[5] A few other recent examples of SAMs incorporating reionization calculations in the literature are Seiler et al. 2019, Visbal, Bryan, Haiman 2020, Hutter et al. 2021.

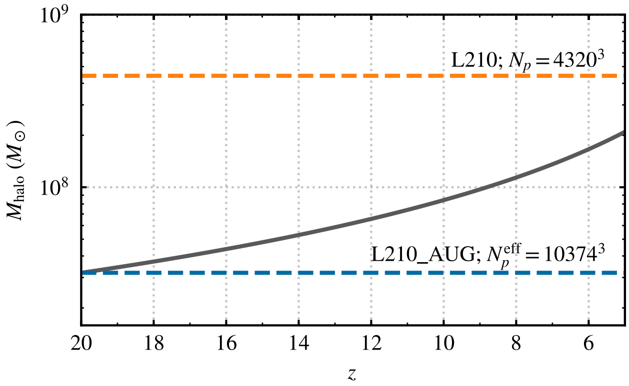

Figure 1. The mass of atomically cooled haloes (dark grey curve) as a function of redshift z along with the representative halo mass resolution of the L210 (orange dashed) and L210_AUG (blue dashed) simulations.

DARKFOREST uses an updated prescription of Benson, Cannella & Cole (2016) for augmenting merger trees and works on what are termed 'simple branches' – merger tree branches that are composed of a halo and all of its immediate progenitors. To add new haloes to the existing merger trees new simple branches are generated using the algorithm outlined in Parkinson, Cole & Helly (2008) which employs a conditional mass function, with extra parametrization (to take care of the differences between the analytic halo mass functions (HMFs) and the ones from N-body simulations) derived from the Extended Press Schechter theory (Bower 1991; Bond et al. 1991; Lacey & Cole 1993). Each halo is split into two (binary splits) in small internal time-steps: we choose these time-steps, dz_1, such that $|dz_1| < <z_1/z_2$ where z_1 is the redshift of the halo and z_2 is the redshift of its immediate progenitors. This construction is repeated until we have an MC merger history. These new MC branches, by construction, have a higher mass resolution than the N-body trees. Building on the methods employed in Benson et al. (2016), the new branches are used to augment the existing N-body merger tree.

For this, we first define a mass threshold, $M_{\rm cut}$, which serves as a dynamic boundary between the N-body and MC halo populations in the final augmented merger tree thus helping us to 'average out' the differences between these two populations. If all the newly added haloes in the generated MC simple branch are less massive than $M_{\rm cut}$ then those haloes are attached to the original N-body simple branch. As a result, the augmented simple branch will have both the MC haloes for $M_{\rm halo} < M_{\rm cut}$ and the original N-body haloes for $M_{\rm halo} > M_{\rm cut}$. The final augmented merger tree with these MC branches grafted onto it will thus have both N-body as well as MC haloes with the $M_{\rm cut}$ serving as the barrier separating the N-body and MC haloes. The resultant 'hybrid' merger tree will have the same mass resolution as the MC simple branches. Benson et al. (2016) used a constant value for $M_{\rm cut}$. We allow $M_{\rm cut}$ to take values $\in [M_{\rm cut}^{\rm min}, M_{\rm cut}^{\rm max}]$. For every simple branch, the augmentation starts with $M_{\rm cut} = M_{\rm cut}^{\rm min}$, but incrementally increases it if the MC simple branch is not deemed fit[6] to be attached to the N-body simple branch. Qiu et al. (2020) used $[M_{\rm cut}^{\rm min}, M_{\rm cut}^{\rm max}] \equiv [100m_{\rm p}, 2500m_{\rm p}]$, where $m_{\rm p}$ is the particle mass of the unaugmented simulation. Instead, we use a $M_{\rm cut}^{\rm min} = 120m_{\rm p}$ taking into account the higher resolution of the L210 simulation while $M_{\rm cut}^{\rm max}$ remains unchanged. This choice was made so that we can retain a larger fraction of the N-body haloes in the L210_AUG simulation. The mass resolution of the augmented simulation is a free parameter of DARKFOREST which we have chosen to be the atomic cooling limit at $z \sim 20$.

In the first column of Fig. 2, we show the HMFs of the augmented (L210_AUG in blue) and unaugmented (L210 in orange) boxes at $z = 8$, 7, 6, and 5. There is a turnover of the HMF of L210 prior to the resolution limit because of the incomplete identification of haloes by the halo-finder. This further motivates the need for augmentation to obtain all the haloes down to the desired mass limit. The HMFs of L210_AUG extend out to the desired mass resolution with the smallest haloes resolved in the augmented tree having a mass of $\sim 2 \times 10^7\,h^{-1}$ M$_\odot$.

Since reionization morphology depends on the location of photon sources, it is important that the positions of the MC haloes are assigned appropriately. DARKFOREST determines the positions and assigns velocities to the newly added MC haloes. We apply the non-linear halo bias prescription from Ahn et al. (2015) on the input dark matter density field from L210 to generate a halo density field. This is normalized and used as a one-dimensional probability distribution from which the MC haloes are assigned their positions by random sampling. The MC haloes are placed uniformly within a voxel in such a way that the number of haloes follows a Poisson distribution. The accuracy of this random sampling method (which we assert by comparing the 2-point correlation functions between the MC and N-body haloes in the same mass ranges) has been shown to depend on the grid size. We performed a convergence test to determine the resolution providing the best performance and use 512^3 cells for our calculations. This is also partly motivated by the resulting grid size of $0.4\,h^{-1}$Mpc being smaller than the H II bubble sizes (Furlanetto et al. 2006a). This method is used to assign positions to every new MC that is not a progenitor of another MC halo (i.e. it has just been resolved for the first time).

The evolution of the MC haloes' position with time is based on their peculiar velocity field, $\boldsymbol{v}(\boldsymbol{x}, t)$, using the linear continuity equation as

$$\nabla \boldsymbol{v}(\boldsymbol{x}, t) = -\frac{1}{\Delta t}[\mathcal{D}(\boldsymbol{x}, t_1) - \mathcal{D}(\boldsymbol{x}, t_2)], \tag{2}$$

where $\mathcal{D}(\boldsymbol{x}, t) = b(M, t)\delta_{DM}(\boldsymbol{x}, t)$ is the halo density field with $b(M, t)$ the linear halo bias (Tinker et al. 2010), and $\delta_{DM}(\boldsymbol{x}, t)$ is dark-matter overdensity field, and Δt is the time-step between the snapshots. Once again, we find that the choice of grid sizes for determining the halo density fields affects the accuracy of the halo positions. Qiu et al. (2020) used an evolving (with z) grid resolution. Based on their results, we use a 256^3 grid resolution at $z = 5$–6, 64^3 at $z = 6$–8, and 32^3 grids at $z > 8$ after compensating for the differences in the simulation volumes.

As detailed in Qiu et al. (2020), we run a number of tests to ensure that the MC haloes are introduced without compromising the accuracy of the underlying L210 simulation. Specifically, while evolving the position of the MC haloes, the 2-point correlation of the halo positions and the velocity distribution of the haloes are checked to ensure they are consistent. The interested reader is referred to Qiu et al. (2020) for a detailed explanation of the augmentation algorithm.

---

[6] This can happen for instance, if the number of MC haloes are less than that of the N-body haloes and/or if the difference in mass of the MC haloes of $M_{\rm halo} > M_{\rm cut}$ and the corresponding N-body haloes in the simple branch are larger than a precision parameter. Note that these MC haloes (with masses above $M_{\rm cut}$) do not end up in the final merger tree but are used solely as a check on the augmentation algorithm. See Qiu et al. (2020) for further details.

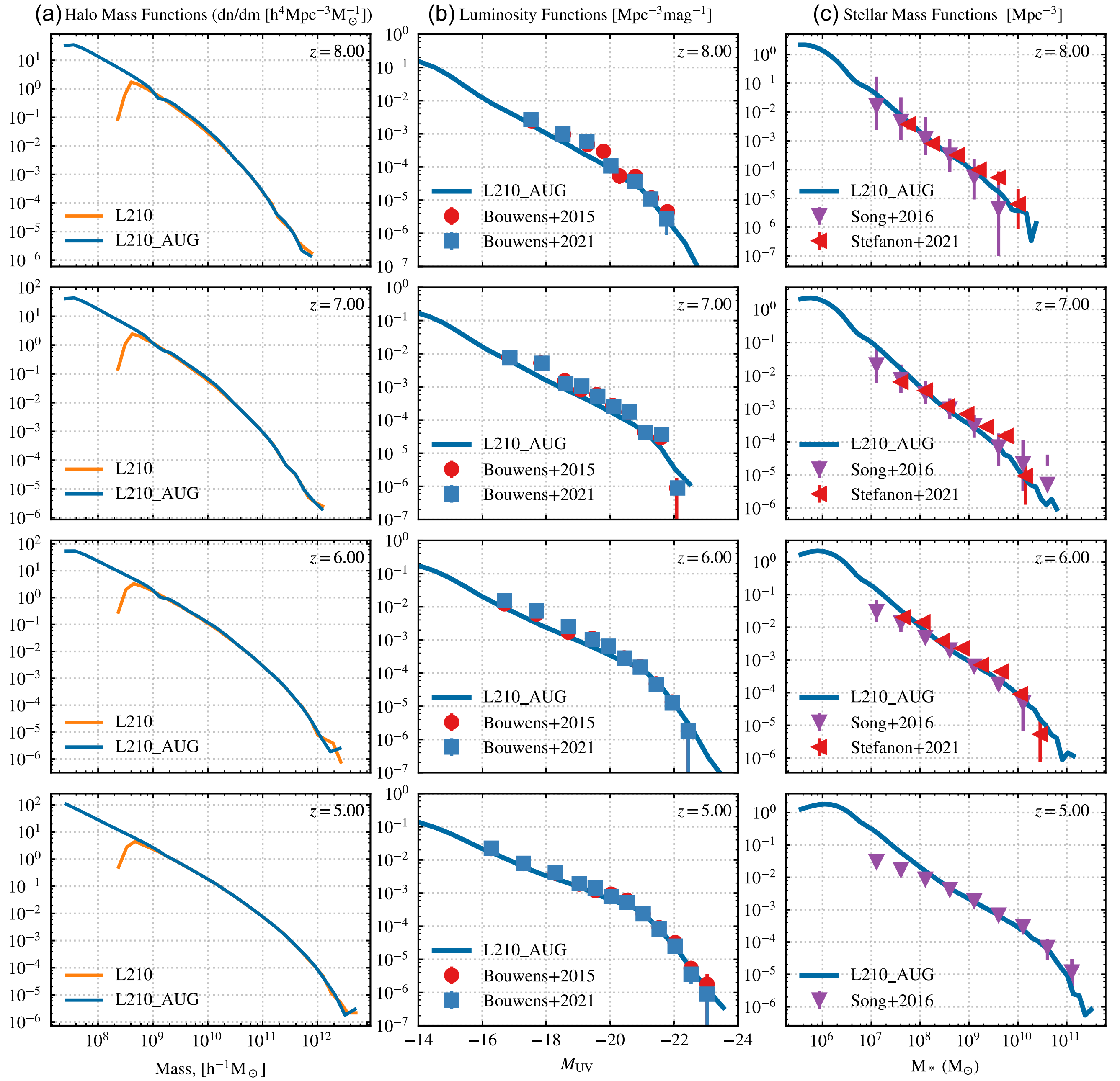

Figure 2. We show the HMF (first column), the LF (middle column), and SMF (right column) at $z \sim 8$, 7, 6, and 5 for both L210 (orange curve) and L210_AUG (blue curve). The first column shows the impact of the augmentation, highlighting the mass of the smallest haloes that are resolved. The final two columns demonstrate the calibration of the MERAXES using existing data. For the LF, we use Bouwens et al. (2015, 2021), and for the SMF, we use Song et al. (2016) and Stefanon et al. (2021).

3 MODELLING GALAXIES AND THE EPOCH OF REIONIZATION

3.1 Galaxy formation using MERAXES

SAMs enable fast and efficient modelling of galaxies and their properties within cosmological volumes. In this work, we use the MERAXES (Mutch et al. 2016) SAM which was specifically designed to study the interplay and feedback between galaxy formation and evolution, and reionization. Since its introduction, MERAXES has undergone several updates. These include AGN feedback (Qin et al. 2017) as well as updates to supernova feedback, recycling and chemical enrichment of the ISM, and reincorporation of the ejected gas (Qiu et al. 2019).

MERAXES includes detailed physically motivated prescriptions for processes including baryonic infall into a dark matter halo, radiative cooling of this infalling gas, star formation, supernova feedback which can heat up the cold gas, mass recycling whereby the ejected material from a supernova can participate in star formation again, metal enrichment of the interstellar medium (ISM), and reincorporation of the gas that is ejected from the galaxy but still bound to the dark matter halo. The dynamical time of a typical galactic disc at high redshift is ∼10 s of Myr (which is similar to the lifetime of massive stars). Our N-body simulations have therefore been constructed with high cadence (with a mean value of 10 Myr between $z \sim 30$ and 5) and MERAXES also includes time-dependent feedback based on the star formation history.

At each snapshot, the baryonic content of a dark matter halo increases up to $f_b f_{\rm mod} M_{\rm vir}$ in the form of pristine primordial gas. Here, $f_b = \Omega_{\rm b}/\Omega_{\rm m}$ is the baryon fraction of the Universe and $f_{\rm mod}$ is the baryon fraction modifier which couples the feedback of reionization to galaxy formation. This newly acquired baryonic gas is deposited into a shock-heated and quasi-static hot-gas reservoir of the galaxy. The fraction of this hot gas which has a cooling time less than the dynamical time of the halo cools radiatively to a much colder gas cloud. This cold gas then participates in star formation following the Kauffmann (1996) model. The cold gas reservoir can also be depleted by the feedback from supernova and active galactic nuclei (Qin et al. 2017).

Qiu et al. (2019) introduced a dust model into MERAXES facilitating the computation of dust attenuated luminosity functions (LFs). The implementation is based on a dust attenuation model from Charlot & Fall (2000). Within a Bayesian framework, Qiu et al. (2019) explored three parametrizations for dust in MERAXES linked to the SFR, dust-to-gas (DTG) ratio, and gas column density (GCD). In this work, we use the DTG model which depends on the cold gas' metallicity and mass.

To model reionization and investigate the role of photoionization feedback on the high-z galaxies, MERAXES includes a modified version of 21CMFAST (described in the next section; Mesinger et al. 2011; Murray et al. 2020). At each snapshot, once the galaxies are identified and all the associated gas reservoirs are updated appropriately, MERAXES models their impact on the H I in the IGM.

3.2 Reionization in MERAXES

Reionization is incorporated self-consistently in MERAXES using the computationally efficient seminumerical code 21CMFAST. Using perturbation theory, 21CMFAST generates evolved density and velocity fields which are then converted to stellar mass and star formation rate (SFR) grids using a simple parametrization to describe the galaxies. In MERAXES, the first two fields come directly from the N-body simulations thus retaining the non-linear effects of structure formation while the stellar mass grids are computed realistically by MERAXES making use of the full galaxy properties. In this work, we extend the reionization calculations of MERAXES to additionally follow the evolution of the spin temperature, $T_{\rm S}$, of H I by incorporating the heating and ionization of the IGM by X-rays following the same approach taken within 21CMFAST. For all of the reionization calculations, we use a grid resolution of 1024^3 corresponding to a cell resolution of $\sim 0.2\,h^{-1}$ Mpc, which is smaller than the typical size of H II regions during the EoR (Wyithe & Loeb 2004). In this section, we describe the implementation of reionization and thermal evolution in MERAXES.

3.2.1 H I *reionization*

The ionization state of the IGM is determined directly from the stellar mass grids following the excursion-set formalism (Furlanetto, Zaldarriaga & Hernquist 2004). Here, the total integrated number of ionizing photons is compared to the number of neutral atoms plus recombinations within spheres of radius R, centred at location $\boldsymbol{x}$ and redshift z. A simulation cell is flagged as ionized if

$$N_{\rm b*}(\boldsymbol{x}, z|R) N_\gamma f_{\rm esc} \geq N_{\rm atom}(\boldsymbol{x}, z|R)(1 + \bar{n}_{\rm rec})(1 - \bar{x}_e), \tag{3}$$

where $N_{\rm b*}(\boldsymbol{x}, z|R)$ is the number of stellar baryons in the sphere, N_γ is the average number of ionizing photons per stellar baryons, and $f_{\rm esc}$ is the escape fraction of the photons. $N_{\rm atom}(\boldsymbol{x}, z|R)$ is the total number of baryons in the same volume, and $(1 - \bar{x}_e)$ accounts for secondary ionizations caused by the X-ray photons. Sobacchi & Mesinger (2014) have shown that recombinations inside Lyman limit systems can significantly reduce the sizes of H II regions. Following their implementation in 21CMFAST, through a sub-grid prescription, we account for recombinations via the $\bar{n}_{\rm rec}$ term which is the mean number of recombinations. We decrease R from a maximum of 50 Mpc, which is the mean-free path in the IGM post-reionization (Songaila & Cowie 2010; Becker et al. 2021), down to the size of a voxel, $R_{\rm cell}$.

The local ionization state of the IGM is used to evaluate the value of $f_{\rm mod}$ for all the galaxies in the volume. The amount of fresh gas accreted in the next snapshot by the host haloes of the galaxies is then suppressed by a factor of $f_{\rm mod}$ thus enabling MERAXES to couple galaxy evolution with reionization. This gives us a reionization scenario that is self-consistent and regulated by the UV background (UVB). An exploration of the interplay between the galaxies and reionization and its impact on the 21-cm PS (though only in the post-heating regime) with MERAXES is given in Geil et al. (2016).

3.2.2 *Spin temperature field*

The 21-cm signal depends upon the spin temperature $T_{\rm S}$ which quantifies the population ratio of the two H I hyperfine energy levels. $T_{\rm S}$ is sensitive to the thermal state of the IGM which is influenced by the X-ray photons and is given by

$$T_S^{-1} = \frac{T_{\rm CMB}^{-1} + x_\alpha T_\alpha^{-1} + x_c T_{\rm K}^{-1}}{1 + x_\alpha + x_{\rm c}}, \tag{4}$$

where $T_{\rm CMB}$, T_α, and $T_{\rm K}$ are the CMB, colour, and gas kinetic temperatures, respectively, x_α is the Wouthuysen–Field (WF) coupling constant (Wouthuysen 1952 & Field 1958) and x_c is the collisional coupling coefficient. We take $T_\alpha = T_{\rm K}$, and x_c is computed as

$$x_c = \frac{0.0628\ {\rm K}}{A_{10} T_\gamma} \sum_i n_i \kappa^{iH}(T_{\rm K}), \tag{5}$$

where A_{10} is the Einstein spontaneous emission coefficient, and $i \in$ {H I, free electrons (e), free protons (p)} and the κ's refers to the corresponding collisional coefficients. We compute x_α as

$$x_\alpha = 1.7 \times 10^{11} (1 + z)^{-1} S\alpha J_\alpha, \tag{6}$$

where S_α is an order-of-unity correction factor involving atomic physics and J_α (pcm^{-2} s^{-1} Hz^{-1} sr^{-1} where 'p' denotes proper units) is the Ly α background flux. We follow the method outlined in Mesinger et al. (2011) for computing S_α and J_α.

Following 21CMFAST, we compute the gas kinetic temperature $T_{\rm K}$ and the ionized fraction $x_{\rm e}$ at position $\boldsymbol{x}$ and redshift z as:

$$\frac{{\rm d}x_e(\boldsymbol{x}, z)}{{\rm d}z} = \frac{{\rm d}t}{{\rm d}z}[\Gamma_{ion} - \alpha_{\rm A} C x_e^2 n_b f_{\rm H}], \tag{7}$$

$$\frac{{\rm d}T_{\rm K}(\boldsymbol{x}, z)}{{\rm d}z} = \frac{2}{3k_{\rm B}(1 + x_e)} \frac{{\rm d}t}{{\rm d}z} \sum_p \epsilon_p + \frac{2T_K}{3n_b} \frac{{\rm d}n_b}{{\rm d}z} - \frac{T_K}{1 + x_e} \frac{{\rm d}x_e}{{\rm d}z}, \tag{8}$$

where $n_b = \bar{n}_{b,0}(1+z)^3[1+\delta_{nl}(\boldsymbol{x}, z)]$ is the total baryonic number density (H + He), $\epsilon_p(\boldsymbol{x}, z)$ is the heating rate per baryon for process p (in erg s^{-1}), $\Gamma_{\rm ion}$ is the ionization rate per baryon, α_A is the case-A recombination coefficient, C is the clumping factor on the scale of the simulation cells ($C \equiv \langle n^2\rangle/\langle n\rangle^2 = 2$; Sobacchi & Mesinger 2014), $k_{\rm B}$ is the Boltzmann constant, and f_H is the hydrogen number fraction. Equation (8) governs the thermal evolution of the gas and incorporates contributions from Compton heating (first term), adiabatic cooling and heating due to Hubble expansion and structure formation, respectively (second term), and the change in internal energy of the system due to the changing number of particles (third term).

Both $\Gamma_{\rm ion}$ and ϵ_p depend on the angle-averaged specific X-ray intensity $J(\boldsymbol{x}, E, z)$. For a voxel with location $\boldsymbol{x}$ at redshift z, the X-ray intensity at energy E, $J(\boldsymbol{x}, E, z)$, is computed by integrating the comoving X-ray specific emissivity $\epsilon_X(\boldsymbol{x}, E_e, z^{'})$ back along the light-cone as

$$J(\boldsymbol{x}, E, z) = \frac{(1+z)^3}{4\pi}\int_z^\infty dz' \frac{cdt}{dz'}\epsilon_X e^{-\tau}, \tag{9}$$

where $e^{-\tau}$ accounts for the attenuation of the X-ray photons by the IGM, i.e. the probability that an X-ray photon emitted at redshift $z^{'}$ survives till z.

We relate the comoving X-ray specific emissivity $\epsilon_X(\boldsymbol{x}, E_e, z^{'})$, evaluated in the emitted frame where $E_e = E(1+z^{'})/(1+z)$, to the star formation rate density SFRD($\boldsymbol{x}$, E_e, $z^{'}$) in the voxel

$$\epsilon_X(\boldsymbol{x}, E_e, z') = \frac{L_X}{\rm SFR} \times {\rm SFRD}(\boldsymbol{x}, E_e, z'), \tag{10}$$

where L_X/SFR is the specific X-ray luminosity per unit star formation that is capable of escaping the galaxy in units of [erg s^{-1} M$_\odot$$^{-1}$yr].

Unlike 21CMFAST, where the SFRD is calculated from the density field and collapse fraction, we compute the SFRD directly from MERAXES making use of our galaxies' properties. Feedback from reionization can thus alter the star formation rates of galaxies. L_X/SFR is assumed to follow a power law of the form $L_X/{\rm SFR} \propto E^{-\alpha_X}$ where E is the photon energy and is normalized with respect to the soft-band X-ray luminosity as

$$L_{X<2\,{\rm keV}}/{\rm SFR} = \int_{E_0}^{2\,{\rm keV}} dE_e\, L_X/{\rm SFR}. \tag{11}$$

Here, E_0 is a threshold energy that fixes the lowest energy of X-ray photon capable of escaping the galaxy by producing a sharp cutoff in the X-ray spectrum that accounts for where the X-rays are absorbed by the high column density gas within the galaxy.

We thus have three free parameters characterizing the X-ray properties of the galaxies: $L_{X\,<\,2{\rm keV}}$/SFR, E_0, and α_X. In this work, we only vary $L_{X\,<\,2{\rm keV}}$/SFR keeping the other two fixed.[7] We set $\alpha_X = 1$ consistent with the observations of high-mass X-ray binaries in the local Universe (Mineo, Gilfanov & Sunyaev 2012; Fragos et al. 2013; Pacucci et al. 2014). Motivated by Das et al. (2017), we adopt a value of $E_0 = 0.5$ keV throughout this work. The physical interpretation of the upper limit of 2 keV in the integral of equation (11) is that X-ray photons with higher energies have mean-free paths longer than the Hubble length and thus do not interact with the IGM.

3.2.3 Brightness temperature field

The 21-cm brightness temperature field is given by (Furlanetto et al. 2006b):

$$\begin{aligned}\delta T_b(\nu) &= \frac{T_S - T_\gamma}{1+z}(1-e^{-\tau_{\nu_0}}) \\ &\approx 27 x_{\rm H\,I}(1+\delta_{nl})\left(\frac{H}{dv_r/dr + H}\right)\left(1-\frac{T_\gamma}{T_S}\right) \\ &\times \left(\frac{1+z}{10}\frac{0.15}{\Omega_M h^2}\right)\left(\frac{\Omega_b h^2}{0.023}\right)\,{\rm mK},\end{aligned} \tag{12}$$

where T_γ is the background radiation (usually assumed to be the CMB) impinging upon the H I cloud, τ_{ν_0} is the optical depth at the 21-cm transition frequency ν_0, $1+\delta_{\rm nl}$ is the density contrast in the dark matter field ($\delta_{nl} = \rho/\bar{\rho} - 1$), $H(z)$ is the Hubble parameter at the redshift z, and dv_r/dr is the radial derivative of the line-of-sight component of the peculiar velocity.

Below $z \sim 25$, we have three broad periods reflected in the 21-cm signal (Pritchard & Loeb 2012):

(i) WF coupling (Ly α pumping): The radiation from the first stars and galaxies begins to couple $T_{\rm S}$ to $T_{\rm K}$ via the WF effect. This drives the global signal ($\overline{\delta T_{\rm b}}$) into the absorption regime.

(ii) X-ray heating: During the Epoch of Heating (EoH), the IGM is heated by X-rays. The $T_{\rm S}$, which is still tightly coupled to the $T_{\rm K}$, increases above $T_{\rm CMB}$ and the 21-cm GS shows an emission feature. The 21-cm signal also becomes insensitive to the spin temperature ($T_{\rm S} >> T_\gamma$ in equation 12).

(iii) Reionization: As reionization proceeds, the 21-cm signal goes to zero.

All of these epochs are reflected in the 21-cm GS and 21-cm PS. X-rays can have a significant impact on the timing and extent of these periods, most notably the EoH.

As is evident from equation (12), the 21-cm signal depends on the ionization, density, velocity, and spin temperature fields. We compute the H I 21-cm signal from the EoR by efficiently computing 3D grids of 21-cm T_S and ionization fields while the velocity and density fields are sourced from the *N*-body simulation.

Most studies in the literature including galaxy formation focus on the post-heating regime with the simplification that $T_{\rm S} >> T_\gamma$ (Geil et al. 2016; also see Greig & Mesinger 2017 for a detailed analysis of the impact of this assumption). While likely valid during the late stages of the EoR, when the luminous sources have managed to couple the spin temperature to the kinetic temperature, for observations into the Dark Ages and the EoH, this assumption breaks down. The main drivers of heating of the cosmic H I are X-ray photons (Furlanetto et al. 2006a; McQuinn 2012). Large-scale simulations with low-mass resolution are unable to simulate the effects of X-rays since the buildup of the stellar mass is delayed (as we demonstrate in Section 4). We use MERAXES combined with our augmented *N*-body simulations for calculations of the full brightness temperature field including contributions from heating, the spin temperature, recombinations, and peculiar velocities.

3.3 Calibration

Due to the numerous physical processes involved in galaxy formation and evolution, SAMs generally contain a large number of free parameters. In order to determine values for these parameters to ensure that a realistic galaxy population is produced, it requires calibrating the model against a number of existing observations. There are two different sets of calibrations involved in MERAXES –

---

[7] See Greig & Mesinger (2017) for an exploration of E_0 and α_X. The reader is also cautioned that a direct comparison with this work is not straightforward since they do not have a realistic galaxy population.

Table 1. The names, mass resolution, X-ray luminosity, and a brief description of all the simulations used in this work.

Name	Mass resolution $[h^{-1}\,\mathrm{M}_\odot]$	$L_{X\,<\,2\mathrm{keV}}/\mathrm{SFR}$ $[\mathrm{erg\,s^{-1}\,M_\odot{}^{-1}yr}]$	Comments
L210	2.98×10^8	3.16×10^{40}	Fiducial simulation
L210_AUG	2.12×10^7	3.16×10^{40}	Augmented fiducial simulation.
L210_AUG_LOWX	2.12×10^7	3.16×10^{38}	Same as L210_AUG but with 1/100th of the galaxy X-ray luminosity
L210_AUG_HIGHX	2.12×10^7	3.16×10^{42}	Same as L210_AUG but with 100 × of the galaxy X-ray luminosity
L210_NR	2.98×10^8	3.16×10^{40}	L210 without recombinations
L210_AUG_NR	2.12×10^7	3.16×10^{40}	L210_AUG without recombinations

Table 2. The fiducial input parameters and their values used for the simulations listed in Table 1. The first set of these (α_{SF}, $\sum_{\mathrm{SF}}$, η_0, ϵ_0, and γ_{DTG}) are calibrated to the observed LFs and SMFs and control the galaxy properties of MERAXES, while f_{esc} & α_{esc} is calibrated with respect to the reionization constraints. See section 3.3 for more details.

Parameter	Value	Description
α_{SF}	0.10	Star formation efficiency
Σ_{SF}	0.01	Critical mass normalization
η_0	7.0	Mass loading normalization
ϵ_0	1.5	Supernova energy coupling normalization
γ_{DTG}	0.65	Galaxy metallicity scaling of optical depth
f^o_{esc}	0.14	Escape fraction normalization
α_{esc}	0.2	Escape fraction redshift scaling

one for the different galaxy formation parameters and the other for the reionization calculations.[8] We calibrate the L210_AUG simulation by varying the following subset of input parameters of MERAXES: α_{SF}, $\sum_{\mathrm{SF}}$, η_0, ϵ_0, γ_{DTG}, f_{esc}, and α_{esc} (see Table 2 for details). We use the same parameter values for all of our simulations (listed in Table 1).

Qiu et al. (2019) calibrated the galaxy formation parameters of MERAXES against observed luminosity functions (LFs) and colour–magnitude relations at $z \sim 4$–7. In this work, we calibrate our simulations with respect to the LFs and the stellar mass functions (SMFs) in the $z \sim 5$–8 range. We find that, except for the γ_{DTG}, the galaxy parameters from Qiu et al. (2019) give a good fit to the data. Fig. 2(b) shows the dust attenuated luminosity functions for redshifts 8, 7, 6, and 5 along with the observational data points (Bouwens et al. 2015, 2021). Fig. 2(c) shows the stellar mass functions for the corresponding redshifts with observations from Song et al. (2016) and Stefanon et al. (2021). We had to recalibrate the γ_{DTG} (0.65 instead of 1.20; see Table 2 of Qiu et al. 2019) parameter which governs the manner in which dust optical depth scales with the cold gas metallicity of the galaxy. The reason is that we extend our calibrations to brighter regions of the LFs than were available to Qiu et al. (2019) because of their smaller simulation size. We summarize the parameters of MERAXES along with their values which have been used for calibration in Table 2.

The second set of calibrations is for the reionization calculations. The photon budget is influenced by the escape fraction (f_{esc}) of the galaxies which sets the fraction of photons that are able to survive the absorption by dust and neutral gas in and around the galaxies and escape into the IGM. The high-z escape fraction is one of the least constrained parameters in the literature. In this work, we use a prescription that is skewed towards the high redshifts as the shallower potential of the small galaxies at high-z results in more photons escaping their hosts. Additionally, the impact of the Monte Carlo haloes is more relevant at high-z and this implementation helps to bring out the importance of these galaxies. In this work, we use an f_{esc} that evolves with redshift z as:

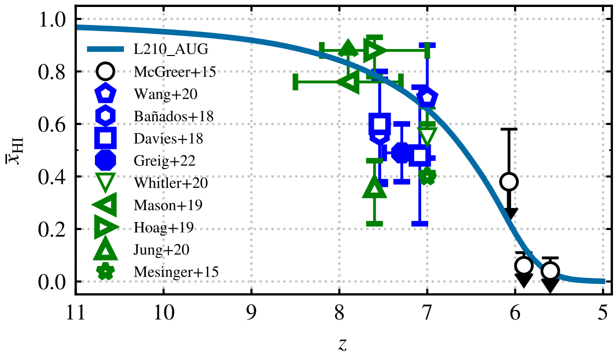

Figure 3. Constraints on the reionization history of the L210_AUG simulation (blue curve). We use an evolving redshift-dependent escape fraction prescription for constraining the EoR history. The observational data are from analyses of dark pixels of Ly α and Ly β forests (McGreer, Mesinger & D'Odorico 2015), and Ly α damping wing absorptions (Mesinger et al. 2015; Bañados et al. 2018; Davies et al. 2018; Mason et al. 2019; Hoag et al. 2019; Whitler et al. 2020; Jung et al. 2020; Wang et al. 2020; Wold et al. 2022; Greig et al. 2022a).

$$f_{\mathrm{esc}} = f^o_{\mathrm{esc}} \left(\frac{1+z}{6} \right)^{\alpha_{\mathrm{esc}}}, \tag{13}$$

where f^o_{esc} is the escape fraction normalization and α_{esc} sets the escape fraction redshift scaling. We tune these parameters such that our reionization history matches the measured constraints on the IGM neutral fractions (Fig. 3) and the integrated optical depth of CMB photons (τ_e) from scattering off free electrons (Fig. 4; Planck Collaboration VI 2020).

4 REIONIZATION PREDICTIONS

In this section, we demonstrate the full reionization model from our L210_AUG simulation. In particular, we focus on comparing the impact of the missing low-mass haloes from the L210 simulation to illustrate the importance of mass resolution.[9]

---

[8] Reionization feedback affects low-mass galaxy formation but not properties constrained by observed LFs (eg. Mutch et al. 2016).

[9] The reader is cautioned that in the current implementation of MERAXES, we are only forming and evolving atomically cooled galaxies and are thus missing the possible contribution from smaller galaxies in molecularly cooled haloes (so-called mini haloes) which are likely to contain PopIII stars. These mini haloes can contribute to the buildup of the background radiation fields and will have an impact on reionization (see for example Qin et al. 2020; Qin et al. 2021; Ventura et al. 2023). Thus, discussions on the appearance of

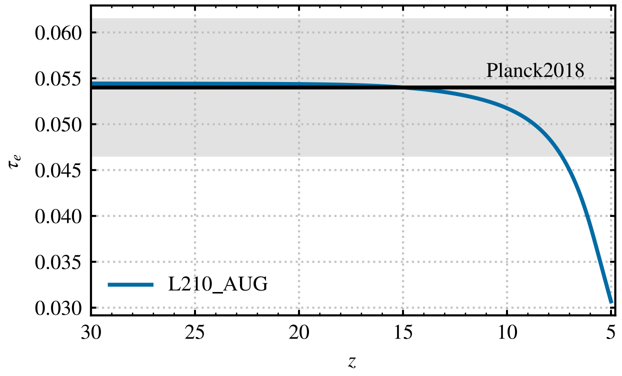

Figure 4. Figure shows the optical depth to CMB photons due to the free electrons. The blue curve is the integrated optical depth (τ_e) computed from the fiducial L210_AUG simulation. The black curve and the shaded region show the most recent measurement of τ_e from the *Planck 2018* collaboration (Planck Collaboration VI 2020).

Since we are missing smaller mass haloes below the mass resolution in L210 we delay the buildup of cosmic stellar mass within galaxies. Thus, there is also a delay in any physical property that is dependent on the total stellar mass (such as ionizations and radiation backgrounds). This will result in the X-ray background forming too late, and correspondingly the IGM cools for longer before heating. However, the L210_AUG simulation includes a realistic galaxy population capable of producing the whole X-ray background. We therefore present here the first large-scale (>200 h^{-1} Mpc) simulation of the thermal and ionization history of the cosmic H I incorporating realistic galaxy formation and evolution physics at masses down to the atomic cooling limit.

As the first application of this simulation, we explore the evolution of the volume-averaged neutral fraction $\bar{x}_{\rm HI}$, the 21-cm GS and the 21-cm PS in this section.

4.1 EoR history and ionization morphology

Fig. 5 shows the resultant EoR histories. As shown in Fig. 3, by construction these resultant reionization histories are consistent with all existing limits and constraints on the IGM neutral fraction during the reionization epoch. The L210_AUG box starts to reionize much earlier than L210 owing to the introduction of low-mass galaxies found only in Monte Carlo haloes. However, the fiducial L210_AUG and L210 simulations both finish reionization at approximately the same redshift. There are two main reasons for this. First, towards the end of the EoR, reionization is primarily maintained by larger mass haloes (which are accurately simulated across both simulations) while the lower mass galaxies are more relevant at earlier times. Secondly, the impact of inhomogeneous recombination in the two simulations is different. Since small galaxies, which initiate reionization in L210_AUG are short-lived, the cosmic gas recombines until sufficiently big galaxies have had time to form and produce enough ionizing photons to complete reionization. In order to check the role of recombination, we therefore ran two additional simulations L210_AUG_NR and L210_NR (shown with dotted lines), where we have turned off inhomogeneous recombinations (i.e. setting $\bar{n}_{\rm rec} = 0$ in equation 3). Turning off inhomogeneous recombination results in L210_AUG_NR reionizing much earlier than L210_NR as expected.

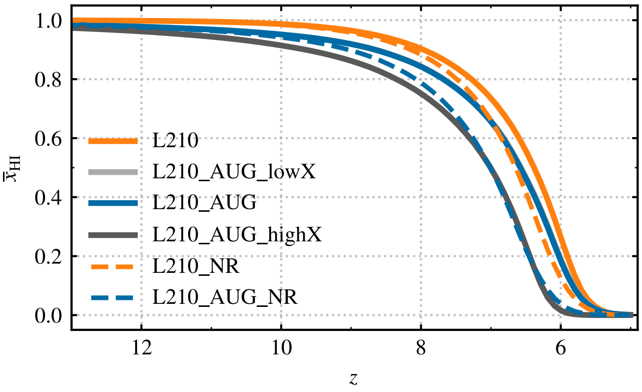

Figure 5. Global reionization history of the L210_AUG (solid blue) and L210 (solid orange) simulations. L210_AUG starts reionizing earlier and also has a much more extended reionization phase. We also vary the galaxy X-ray luminosity in our model (L210_AUG_HIGHX & L210_AUG_LOWX in dark and light grey, respectively). The L210_AUG_LOWX is almost identical to L210_AUG and thus the curves overlap. The two dotted curves are the same as L210_AUG & L210 except that we do not include inhomogeneous recombinations.

Fig. 6 shows slices from the ionization fields of L210_AUG (top row) and L210 (middle row) for $\bar{x}_{\rm HI} \sim 0.75$, 0.50, and 0.25. Each slice is 210 h^{-1} Mpc on a side and $\sim$0.2 h^{-1} Mpc thick. In order to emphasize the effects of the introduction of the small haloes, we compare the simulations at the same volume-averaged neutral fractions ($\bar{x}_{\rm HI}$). At any given $\bar{x}_{\rm HI}$, there will be more small haloes in L210_AUG compared to L210. One of the main impacts of the smaller haloes is to force reionization to begin earlier as discussed above. Thus, on average, the large ionized regions in L210_AUG are smaller as they are driven by lower stellar masses relative to the L210 simulation as indicated by the earlier redshift for a fixed neutral fraction. The third row shows the difference between the two simulations with the colour gradient chosen to highlight the contribution from the extra small mass haloes. In the ‘Difference’ (bottom row), we have subtracted the ionization fields of L210_AUG from L210 to clearly bring out the impact of the augmentation.

4.2 21-cm statistics

Fig. 8 shows the 21-cm GS for L210_AUG and L210. We find that the L210_AUG simulation has a similar (but broader) absorption feature, though occurring earlier in redshift, relative to L210. This highlights the importance of introducing the low-mass haloes beyond the resolution limit of L210. By including these in L210_AUG, the Ly α and X-ray background builds up at earlier times due to the additional low-mass haloes. The Ly α background couples the spin temperature to the gas kinetic temperature $T_{\rm K}$, which is much lower than the CMB temperature $T_{\rm CMB}$, resulting in the broader and earlier absorption. We also point out that the gradient of the absorption feature in the 21-cm GS is larger in L210 as compared to L210_AUG. The delayed but sudden formation of sources in L210, relative to L210_AUG, results in a comparatively rapid buildup of the stellar mass and consequently the radiation backgrounds.

Fig. 9 compares the evolution of the spherically averaged 3D 21-cm PS at fixed spatial scales ($k \sim 0.1\,{\rm Mpc}^{-1}$ and $k \sim 1\,{\rm Mpc}^{-1}$) for the L210 and L210_AUG simulations. For both of these scales, the evolution of the power for L210 is qualitatively similar to L210_AUG.

---

features in this work will also be delayed relative to simulations which also include mini haloes.

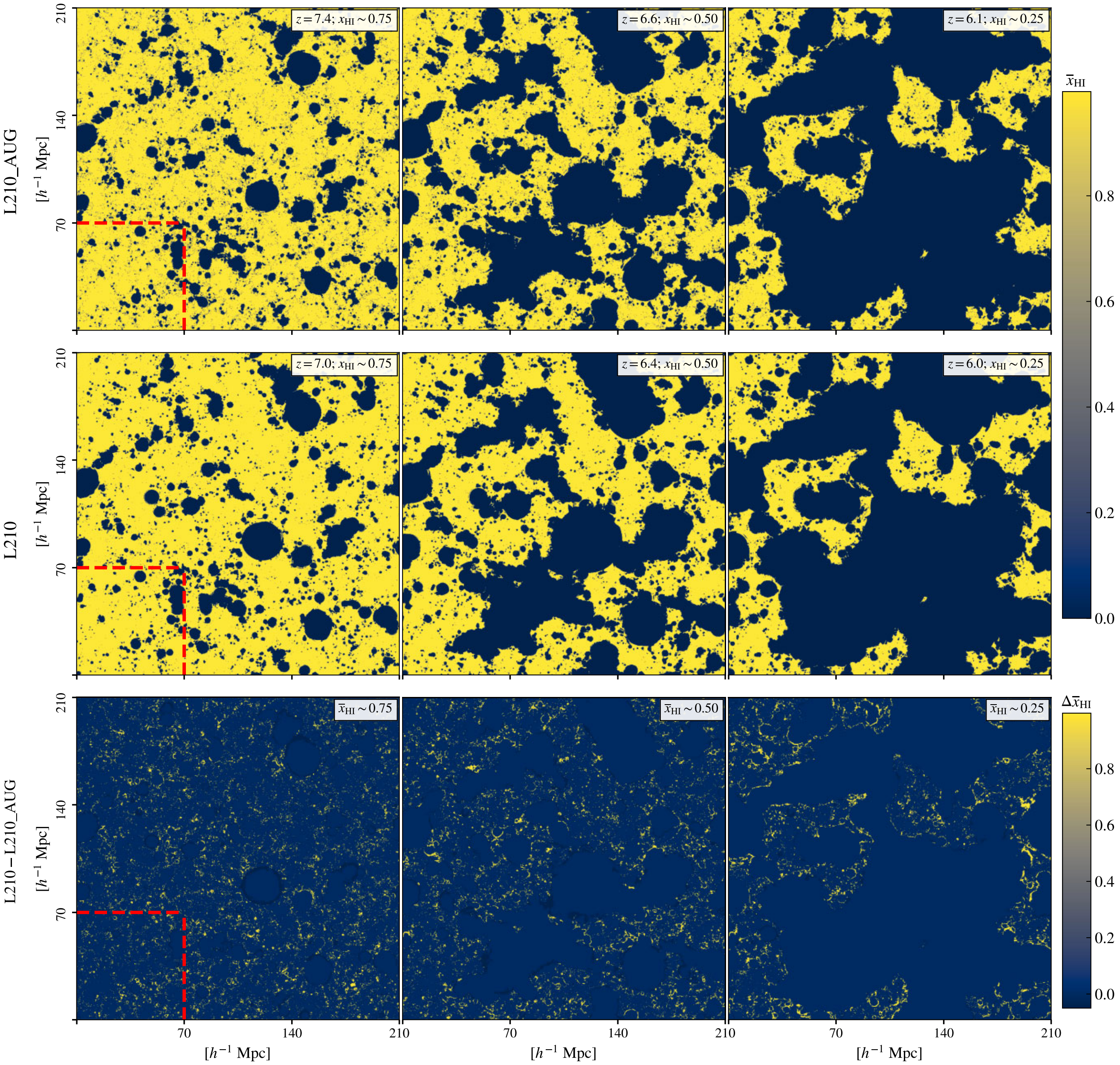

Figure 6. 2D slices of the $\bar{x}_{\rm HI}$ grid from the L210_AUG (upper row) and L210 (bottom row) simulations. From left to right, the columns correspond to fixed neutral fractions, $\bar{x}_{\rm HI} \sim 0.75, 0.5, 0.25$. For a particular $\bar{x}_{\rm HI}$, L210_AUG has a higher redshift compared to L210 because of the higher number of ionizing photons. Yellow represents neutral hydrogen (H I), and blue regions are ionized hydrogen (H II) bubbles. Each slice is 210 h^{-1} Mpc on a side and $\sim$0.2 h^{-1} Mpc thick. The last row shows the difference between the ionization fields of the two simulations ($\Delta\bar{x}_{\rm HI} = \bar{x}_{\rm H\,I,L210} - \bar{x}_{\rm H\,I,L210\_AUG}$). We have used a colour gradient that is weighted towards the small scale structures to highlight the small H II regions that are due to the Monte Carlo haloes. The red dashed regions in the first column show the size of our 70 h^{-1} Mpc side-length sub-volumes (see Section 5 for further details).

However, the delayed formation of stellar mass in L210 results in there being considerable differences between the timing of the peaks. The Ly α-coupling peak in L210 is delayed relative to L210_AUG by $\Delta z \sim 3$. Below $z \sim 7$, when the X-rays have already initiated the EoH and EoR is well on its way, the power in both L210_AUG and L210 becomes similar.

Even though the large-scale ($k \sim 0.1\,{\rm Mpc}^{-1}$) 21-cm power is expected to have three peaks corresponding to the Ly α-pumping, X-ray heating, and reionization epochs (see Pritchard & Furlanetto 2007; Mesinger, Ferrara & Spiegel 2013) we observe only two peaks in our simulations. The EoH peak, expected at $z \sim 12$ for L210_AUG (corresponding to the minima of the global signal; see Fig. 8) is masked by the Ly α peak. They have merged together into one broad peak owing to the timing and buildup of the backgrounds during these two epochs.[10]

On the other hand, the redshift evolution of the 21-cm power on small-scales ($k \sim 1\,{\rm Mpc}^{-1}$) is characterized by two peaks corresponding to a combined Ly α-pumping and EoH, and an EoR

---

[10] Another contributing factor is the slow buildup of the backgrounds owing to the time-scales of ionizing photons (as evidenced by the different gradients of the global signals).

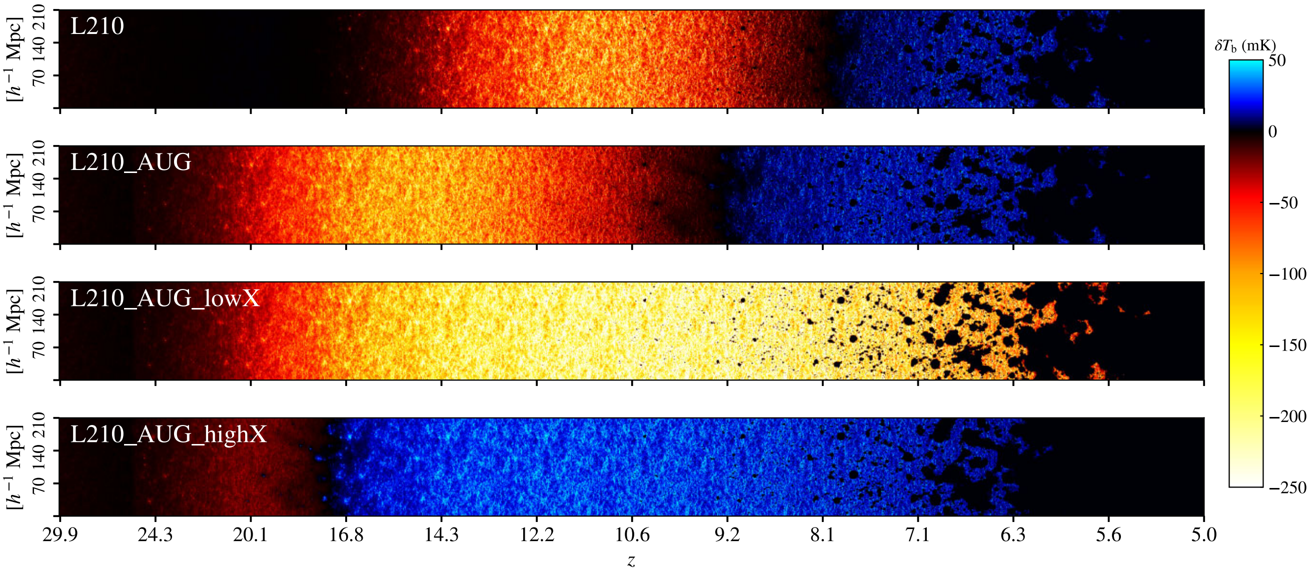

Figure 7. The light-cone evolution of the 21-cm brightness temperature (δT_b) from our simulations. L210 is characterized by the delayed but rapid evolution of δT_b because of its lower resolution. We also point out L210_AUG_LOWX, characterized by low galaxy X-ray luminosity, in which the cosmic H I remains cold and never goes into emission.

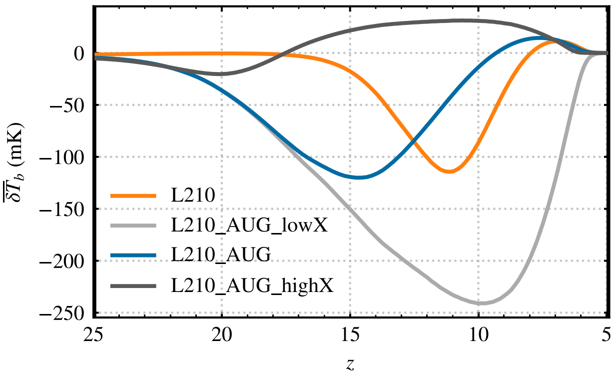

Figure 8. Figure shows the effect of X-rays on the 21-cm GS from the cosmic dawn and EoR. As expected, more X-rays (dark grey) cause the signal to be observed in emission earlier whereas a lack of X-rays (light grey) causes a deeper absorption feature.

peak (Qin et al. 2020). Typically, on small scales, the impact of the EoH is harder to disentangle as it primarily impacts larger scales due to the larger mean free path of X-ray photons.

4.3 Effects of varying the Galaxy X-Ray Luminosity in the early Universe

The large volume of our simulations enables the exploration of the effects of X-rays on the EoR morphology with a full source population. Here, we only vary $L_{X<2\,\mathrm{keV}}$/SFR, keeping E_0 and α_X fixed. In addition to our fiducial value of $3.16\times10^{40}\,\mathrm{erg\,s^{-1}\,M_\odot^{-1}\,yr}$, we also consider 3.16×10^{38} and $3.16\times10^{42}\,\mathrm{erg\,s^{-1}\,M_\odot^{-1}\,yr}$ which we call L210_AUG_LOWX and L210_AUG_HIGHX simulations, respectively (see Table 1). This enables us to encompass the plausible range of contribution of the X-rays in the early Universe (Fialkov et al. 2017; Greig & Mesinger 2017). Fig. 7 shows the light-cone evolution (of δT_b) for these simulations. We note that The HERA Collaboration et al. 2022 have recently ruled out a number of 'cold reionization' models corresponding to low-X-ray luminosity. In light of this, our L210_AUG_LOWX model is a very unlikely scenario. However, our aim in this work is to develop an intuition for the impact of X-rays in the early Universe from a galaxy SAM and reionization simulation.

In the next subsections, we compare the impact of the X-ray photons in the early Universe relative to our fiducial model.

4.3.1 EoR history

The ionization photon budget is dominated by UV photons, with the X-rays contributing at most 10–15 per cent in the most extreme models (Mesinger et al. 2013). Fig. 5 shows the reionization histories from all three of the augmented simulations. We find that, in agreement with studies in the literature (Mesinger et al. 2013), though the role of X-rays in ionizing the H I is much less than that of the UVB, they can hasten reionization (see L210_AUG versus L210_AUG_HIGHX in Fig. 5).

4.3.2 21-cm light-cone

In Fig. 7, we show the 21-cm brightness temperature (δT_b) light-cone slices from our simulations. The 21-cm signal, being a line transition, evolves along the line of sight and light-cones provide a realistic representation of the evolution of such cosmic signals. We stitch together the δT_b grids from our coeval simulation boxes to generate the ligh-cone by linearly interpolating them in cosmic time between snapshots. The delayed but rapid evolution in the case of L210, compared to the rest of the simulations, underscores the impact of the mass resolution on the 21-cm signal. For L210_AUG_LOWX, the signal remains in absorption across our full redshift range whereas for L210_AUG_HIGHX, it is mostly in emission.

4.3.3 21-cm global signal

Fig. 8 shows the 21-cm GS from all four simulations. As shown in Section 4.3.2, the main physical impact of X-ray photons is to heat the cosmic gas. With respect to our fiducial L210_AUG simulation, L210_AUG_LOWX simulation has less X-ray photons resulting in

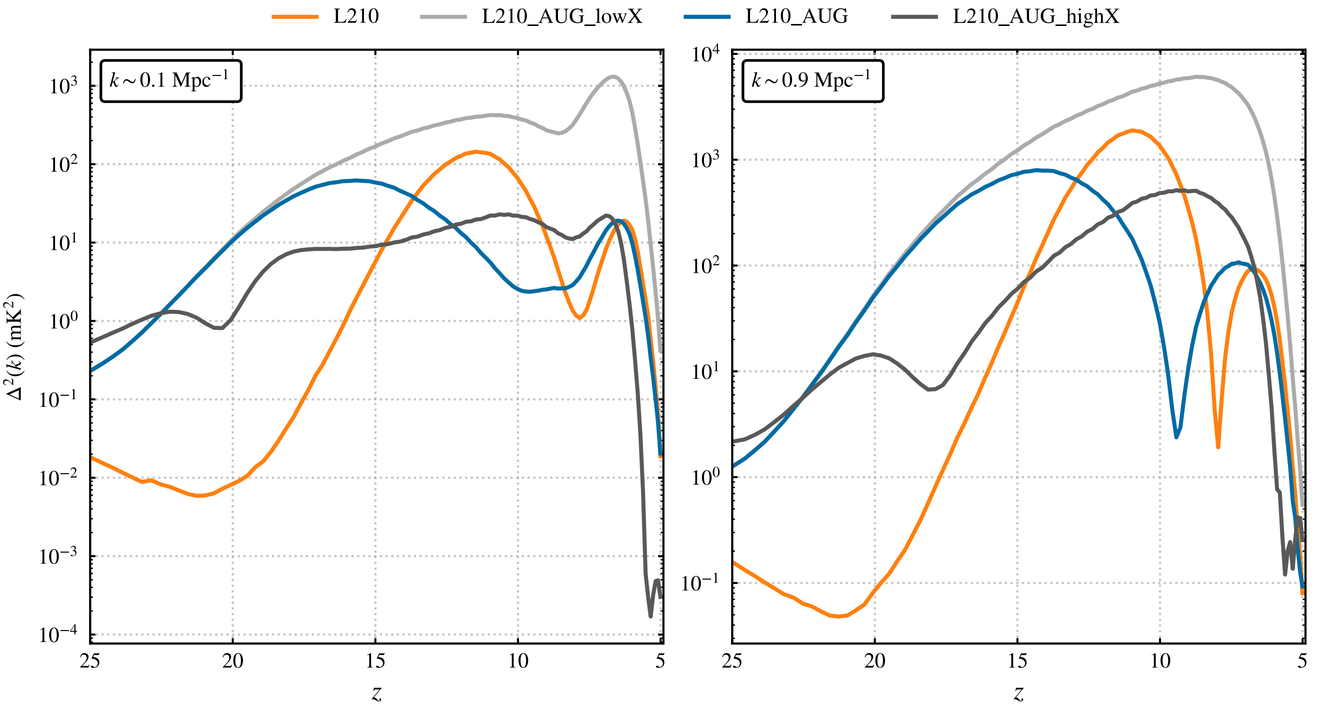

Figure 9. We show the 21-cm power spectra for the simulations at two scales ($k \sim 0.1$ Mpc^{-1} on left and $k \sim 1$ Mpc^{-1} on the right).

the cosmic gas being colder, and hence a stronger absorption dip. All of our simulations except L210_AUG_LOWX go into emission (also evident from Fig. 7). L210_AUG_HIGHX, being characterized by significantly more X-ray photons than the other simulations, has a hot IGM resulting in the signal going into emission at $z \lesssim 17$ as well as the merging of the Ly α-pumping epoch with the EoH.

4.3.4 21-cm power spectra

In Fig. 9, we compare the evolution of the 21-cm PS at $k \sim 0.1$ Mpc^{-1} and $k \sim 1$ Mpc^{-1}. Like the 21-cm GS, the shape and amplitude of the 21-cm PS are strongly affected by the X-ray luminosity. An accurate measurement of the 21-cm PS will thus have great constraining power on the properties of the X-ray sources in the early Universe (see e.g. the recent constraints from The HERA Collaboration et al. 2022).

At large scales (left-hand panel of Fig. 9), we observe the expected features, though there is considerable variation in the timing and duration among the simulations. We note that the L210_AUG_LOWX simulation has the highest power for most epochs (with peak power during the EoR at $z \sim 7$) owing to the large temperature contrasts due to the cold IGM. The inefficient heating because of the low-X-ray luminosity has also resulted in the EoH and EoR peaks merging together. L210_AUG simulation shows the 3 expected peaks with the power peaking at $z \sim 16$ corresponding to the absorption in the 21-cm GS; there is thus more power during the Ly α-pumping epoch. L210_AUG_HIGHX is characterized by less power during all epochs. Though the general features are similar to the L210_AUG simulation, the amplitude and timing are different due to the reduction in the amplitude of the IGM temperature contrast. The L210_AUG_HIGHX simulation is characterized by much smaller temperature fluctuations than the other two simulations. Thus, during the EoH, this simulation has the smallest amplitude.

The right-hand panel shows the power on small scales. The power on this scale exhibits the expected behaviour. Interestingly, L210_AUG_HIGHX has clearly differentiated Ly α-pumping and EoH peaks. The EoH peak in this case has merged with the EoR peak, owing to the extended EoH because of the large X-ray luminosity.

5 COSMIC VARIANCE IN EOR STATISTICS

Measurement of any statistical signal from a finite volume of the Universe introduces an inherent uncertainty in its variance since we are only sampling one realization of the underlying statistical ensemble. This is termed the *cosmic variance*. In this section, as an application of our large volume simulations, we explore the cosmic variance of the 21-cm signal.

To explore the cosmic variance, we divide each of the augmented simulations into 27 equal sub-volumes each of side 70 h^{-1} Mpc. Each sub-volume is larger than the typical largest ionized regions even during the late stages of reionization. The 70 h^{-1} Mpc sub-volumes are also comparable to most state-of-the-art radiation hydrodynamical simulations in the literature (Kaurov & Gnedin 2015; Feng et al. 2016; Springel et al. 2018; Ocvirk et al. 2020; Kannan et al. 2022) and also to the largest simulation volume on which MERAXES has been run (Qiu et al. 2019) as part of the DRAGONS project. Our ensemble therefore provides an estimate of the cosmic variance in these simulations.

5.1 EoR history and 21-cm global signal

Fig. 10 shows the spread in the reionization histories for the different sub-volumes (in light blue) relative to L210_AUG (in blue). We find that the range in redshift for reionization histories among sub-volumes at $\bar{x}_{\mathrm{HI}} \sim 0.5$ is $\Delta z \sim 0.8$. The bottom panel shows the standard deviation of $\bar{x}_{\mathrm{HI}}$ ($\sigma(\bar{x}_{\mathrm{HI}})$) among the sub-volumes. We

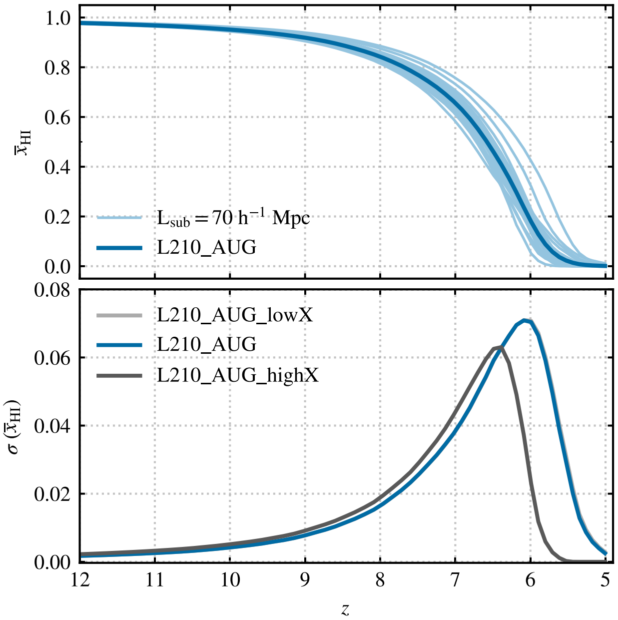

Figure 10. The blue curve shows the EoR history of the L210_AUG simulation and the lighter shades show the EoR history in the 27 sub-volumes which the L210_AUG has been divided into. We find a spread in the EoR history with almost $\Delta z \sim 0.8$ around $\bar{x}_{\rm HI} \sim 0.5$. The bottom panel shows the standard deviation of the $\bar{x}_{\rm HI}(\sigma(\bar{x}_{\rm HI}))$ among the sub-volumes and we show this for all the augmented simulations. The L210_AUG_LOWX (light grey) curve is identical to the L210_AUG curve and lies behind it.

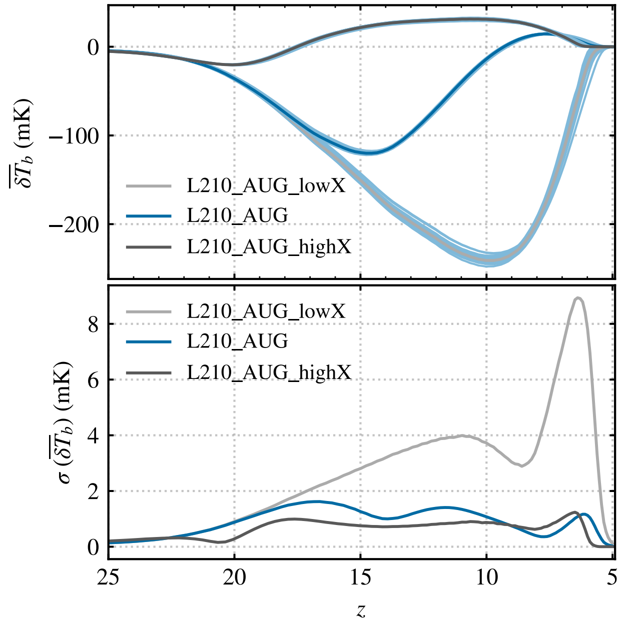

Figure 11. The evolution of the 21-cm GS among the sub-volumes (light blue) for all three of the augmented simulations. The bottom panel shows the standard deviation of the global signal among the 27 sub-volumes.

see the same trend among the simulations except that features in the L210_AUG_HIGHX simulation occur earlier relative to the L210_AUG and L210_AUG_LOWX simulations (which are almost identical).

In Fig. 11, we do a similar analysis for the 21-cm GS with the top panel showing the signal from the sub-volumes and the bottom panel showing the standard deviation. Comparing the bottom panels of Figs. 10 and 11, we see that the fractional change in $\overline{\delta T}_{\rm b}$ is higher than in $\bar{x}_{\rm HI}$. During the EoH, the scatter in $\delta T_{\rm b}$ is driven by variations in $T_{\rm S}$ while during reionization the scatter in $\bar{x}_{\rm HI}$ dominates.

5.2 21-cm Power Spectra

Fig. 12 shows the 21-cm PS from the L210_AUG simulation (in blue) at $\bar{x}_{\rm HI} \sim 0.95$, 0.8, 0.70, 0.60, 0.30, and 0.10. The 21-cm PS from the 27 sub-volumes (in light blue) are also shown. The scatter in the 21-cm PS increases for decreasing k-value (towards large scales) and decreasing redshift (as reioniszation progresses). The spread in power for large k-values is larger than the spread at small k-values for all redshifts. This is due to sample variance since there are fewer modes at these large scales in the volumes to average over. At low redshifts, most of the 21-cm emission comes from sparse, isolated neutral patches leading to considerable scatter in the 21-cm power.

The power spectrum quantifies the variance in amplitudes of a random field on different scales. A purely Gaussian-random field is fully specified by its power spectrum (Peebles 1980). The cosmic variance of the power spectrum in this case should simply be the Poisson sampling error which depends only on the number of modes in each spherical shell in k-space. However, higher order statistics are required to capture the information for non-Gaussian fields.

The 21-cm field is non-Gaussian, especially on small scales and during the final stages of the EoR. Initially, the 21-cm emission traces the underlying matter density field which is Gaussian on large scales where the evolution is governed by linear theory. However, once the complex 3D morphology of the radiation fields (e.g. ionization, X-ray, or Lyman-alpha) begins to impact the 21-cm signal, the statistics will deviate from Gaussianity (Morales & Wyithe 2010). Hence, the cosmic variance of the 21-cm power spectrum will be larger than the Poisson sampling error. Here, we explore the impact of non-Gaussianity on the cosmic variance uncertainty of the 21-cm PS.

Mondal, Bharadwaj & Majumdar (2016) showed that non-Gaussianity has an appreciable impact on the error-covariance of the power spectra. The full error-covariance matrix of the 21-cm PS is given by

$$\boldsymbol{C}_{ij} = \frac{1}{V}\left[\left(\frac{(2\pi)^2[\overline{P}(k_i)]^2}{k_i^2\Delta k_i}\right)\delta_{ij} + \overline{T}(k_i, k_j)\right], \tag{14}$$

where V is the simulation volume, k_i is the average spatial frequency in the ith bin, Δk_i is the bin-width of the ith bin, $\overline{P}(k_i)$ is the power spectrum averaged over the ith bin, and $\overline{T}(k_i, k_j)$ is the average trispectrum. This trispectrum component arises from the non-Gaussianity of the 21-cm signal.

Generally, studies in the literature make the simplifying assumption that the 21-cm field is Gaussian and ignore the second term in equation (14) giving

$$\begin{aligned}\delta P(k_i) &= \sqrt{\boldsymbol{C}_{ii}}\\ &= \sqrt{\frac{(2\pi)^2[\overline{P}(k_i)]^2}{V k_i^2 \Delta k_i}}.\end{aligned} \tag{15}$$

Hence, any deviation from equation (15) measured from our 27 sub-volumes must occur as a result of the non-Gaussianity of the 21-cm signal.

From each of the 27 equal sub-volumes, we compute the spherically averaged power spectrum and show in Fig. 13, the ratio of

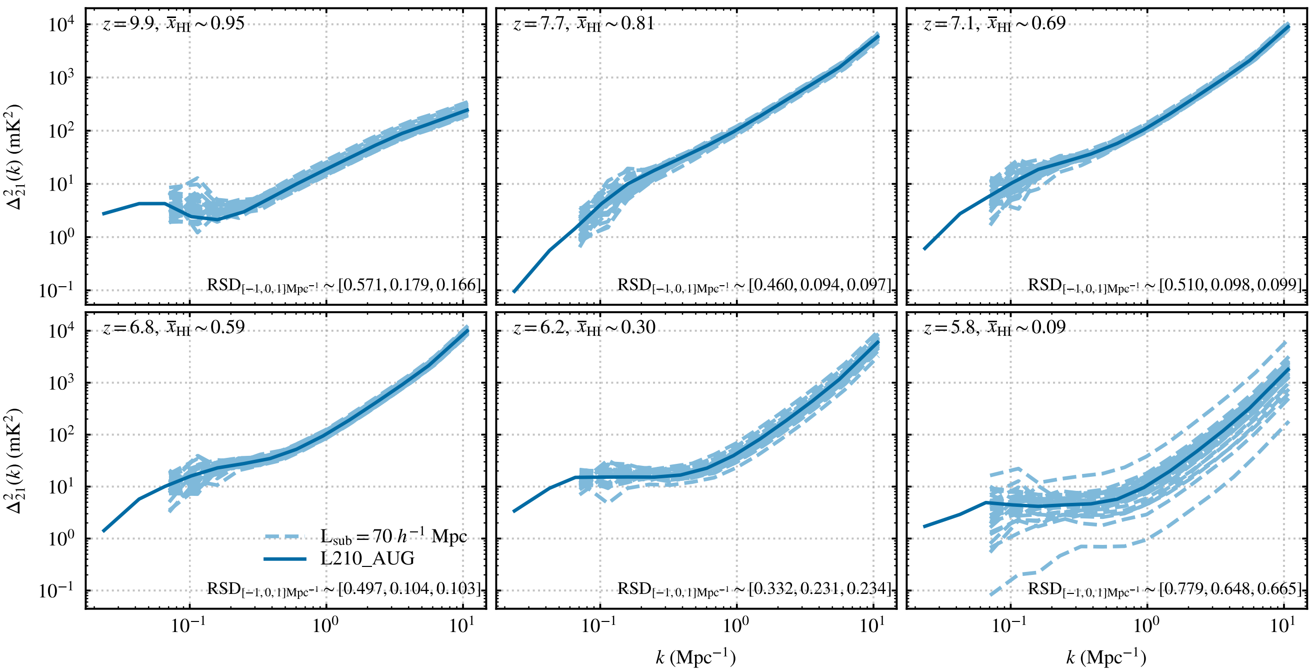

Figure 12. The fiducial augmented simulation L210_AUG has been subdivided into 27 equal sub-volumes. Shown (dashed light blue) here are the 21-cm power spectra from these sub-volumes. The power spectra from the whole volume are also shown (solid blue). The subplots correspond to $\overline{x}_{\rm HI} \sim 0.95, 0.8, 0.70, 0.50, 0.30, 0.10$. We also show the relative standard deviation (RSD $= \frac{\text{standard deviation}}{\text{mean}}$) of the powers at $k = 10^{-1}$, 10^0, and 10^1 Mpc^{-1} spatial scales from the sub-volumes.

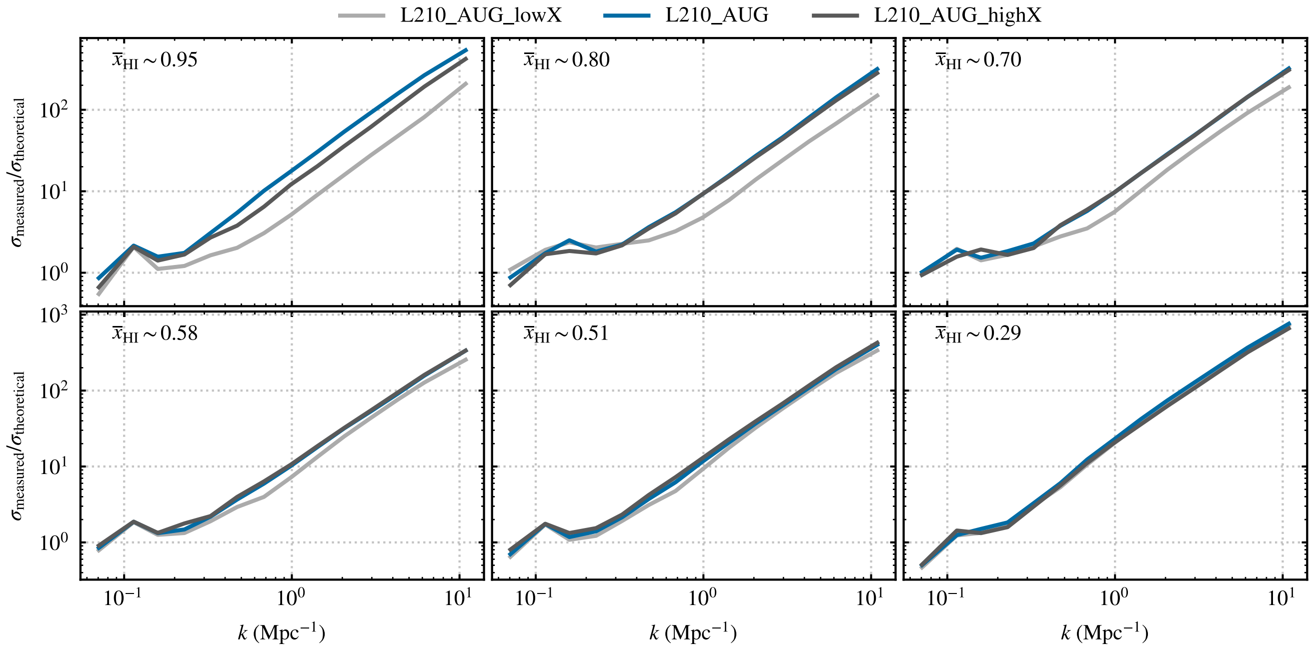

Figure 13. Figure shows the ratio of measured to theoretical errors. We compute the standard deviation of the power among the 27 sub-volumes as a function of k, $\sigma_{\rm measured}$. We compare this with the $\sigma_{\rm theoretical}$, where we use the mean of the powers among the sub-volumes as the $\overline{P}(k_i)$ in equation (15).

the measured cosmic variance from the sub-volumes ($\sigma_{\rm measured}$) to that expected theoretically from equation (15) ($\sigma_{\rm theoretical}$). Specifically, $\sigma_{\rm measured}$ is computed as the standard deviation of the power among the sub-volumes as a function of k, while $\sigma_{\rm theoretical}$ is computed using equation (15), where the $\overline{\rm P}(k_i)$ is the mean 21-cm PS from the sub-volumes. For a Gaussian field, we expect the ratio $\sigma_{\rm measured}/\sigma_{\rm theoretical}$ to be unity. We provide this ratio for $\overline{x}_{\rm HI} \sim 0.95$, 0.75, 0.50, and 0.25 in each of our three augmented simulations.

We find similar features and trends among all of our simulations. The ratio[11] increases from small to large k-values implying that

---

[11] At the same time, we caution that it is possible we overpredict the cosmic variance due to the smaller size of our sub-volumes. Our sub-volumes are

the large-scales are more Gaussian in nature compared to the small scales.

Our results agree qualitatively with Mondal et al. (2015, 2016) who show that the non-Gaussianity of the 21-cm field grows with the progress of reionization. During the early stages of the EoR ($\bar{x}_{\rm HI} \sim 0.80$ case), we find that the contribution of non-Gaussianity to the variance of the 21-cm PS is comparable to the Gaussian term for $0.1 \lesssim k \lesssim 0.4\,{\rm Mpc}^{-1}$ (where the ratio $\sigma_{\rm measured}/\sigma_{\rm theoretical} \sim \mathcal{O}(1)$) while for $k \gtrsim 2\,{\rm Mpc}^{-1}$ the ratio is >10. As EoR progresses (see $\bar{x}_{\rm HI} \sim 0.30$ subplot), this ratio becomes 2–4 for $0.1 \lesssim k \lesssim 0.4\,{\rm Mpc}^{-1}$ and up to $\sim$100 for $k \gtrsim 2\,{\rm Mpc}^{-1}$. At the same time, we find that the transition to non-Gaussianity in our model appears to occur earlier than in Mondal et al. (2016). Likely, this is a result of the detailed physics prescription of our model, making a direct comparison hard particularly at high redshifts since our simulations include spin temperature fluctuations which likely add to the non-Gaussianity in the 21-cm signal.

Our results show that when estimated by assuming that the 21-cm field is Gaussian (i.e. using equation 15), towards the end of EoR, the cosmic variance within $\sim$100 Mpc boxes is underestimated by a factor of $\sim$2 within $k \sim 0.1$–$0.5\,{\rm Mpc}^{-1}$ scales which are the main focus of the current and upcoming telescopes observing 21-cm fluctuations.

6 CONCLUSION

In this paper, we have introduced an updated version of the MERAXES semi-analytic model, which for the first time includes heating from X-rays and thermal evolution of gas in the IGM. In order to have sufficient volume for calculating the effect of X-rays during reionization, we utilize a new large-volume *N*-body simulation with sidelength $L = 210\,h^{-1}\,{\rm Mpc}$ and 4320^3 particles (L210). To resolve all atomically cooled haloes out to $z = 20$ necessary for studying galaxy formation (of $\sim 2 \times 10^7\,h^{-1}\,{\rm M}_{\odot}$), we performed Monte Carlo augmentation of this simulation using DARKFOREST (L210_AUG). This achieves an effective *N*-body particle number of $\sim 10\,000^3$. L210_AUG is a unique data set for exploring galaxy formation physics and its impact on the timing and morphology of the EoR. Coupling MERAXES to this augmented simulation enables the exploration of the different galaxy formation parameters on the 21-cm signal. We found that the inclusion of these Monte Carlo haloes has a significant impact on the buildup of stellar mass in our simulations and consequently on reionization, which commences earlier and is more gradual. We also find that Ly α-coupling and X-ray heating, and hence, the end of the 21-cm global minima occur earlier in the higher resolution simulation. In addition, we find that the timing and duration of the peaks of the 21-cm power spectrum (PS) are different in the augmented higher resolution simulation. These results underscore the need for both large volume and sufficient mass resolution for simulations exploring the EoR.

The large volume of our simulation and the implementation of thermal and spin temperature evolution in MERAXES enables exploration of the impact of X-ray luminosity on heating the H I gas. In agreement with seminumerical studies (Mesinger et al. 2013; Greig & Mesinger 2017), we show that while their impact on the reionization history is minimal, X-rays can have an appreciable impact on both the 21-cm GS and on the 21 PS. Observations of the 21-cm PS will thus provide constraints on the X-ray properties of the sources in the early Universe.

Taking advantage of the large volume of our simulation, we explore the scatter in the reionization history and the 21-cm global signal within 27 sub-volumes of side $70\,h^{-1}\,{\rm Mpc}$, which are each comparable to our previous simulations and state-of-the-art radiation hydrodynamical simulations in the literature. We compare the standard deviation in the 21-cm PS amongst these sub-volumes to the Gaussian expectation for the variance of a random field. As previously described in Mondal et al. (2016), we find that the non-Gaussianity of the signal contributes significantly to the variance of the 21-cm PS on all scales and increases towards the small scales. However, this work is the first study of the error-variance of the 21-cm PS at high redshifts in a model that also includes both a model of galaxy formation and spin temperature fluctuations. We find that the assumption of Gaussianity for the 21-cm field results in underestimating the cosmic variance of the 21-cm PS by a factor of $\gtrsim$2 for the scales relevant for the SKA ($k \sim 0.1$–$0.5\,{\rm Mpc}^{-1}$).

Software citations:

(i) PYTHON (Van Rossum & Drake Jr 1995)
(ii) NUMPY (Harris et al. 2020)
(iii) SCIPY (Virtanen et al. 2020)
(iv) MATPLOTLIB (Hunter 2007)
(v) CYTHON (Behnel et al. 2011)
(vi) CORRFUNC (Sinha & Garrison 2020)

ACKNOWLEDGEMENTS

We thank the referee for their detailed comments which improved the quality of this manuscript. This research was supported by the Australian Research Council Centre of Excellence for All Sky Astrophysics in 3 Dimensions (ASTRO 3D), through project #CE170100013. Part of this work was performed on the OzSTAR national facility at the Swinburne University of Technology. The OzSTAR program partially receives funding from the Astronomy National Collaborative Research Infrastructure Strategy (NCRIS) allocation provided by the Australian Government. This research was also undertaken with the assistance of resources from the National Computational Infrastructure (NCI Australia), an NCRIS-enabled capability supported by the Australian Government. YQ acknowledges ASTAC Large Programs and the Research Computing Services NCI Access scheme at The University of Melbourne for some NCI computing resources.

DATA AVAILABILITY

The data underlying this article will be shared on reasonable request to the corresponding author.

REFERENCES

Ahn K., Iliev I. T., Shapiro P. R., Srisawat C., 2015, MNRAS, 450, 1486
Bañados E. et al., 2018, Nature, 553, 473
Barkana R., Loeb A., 2001, Phys. Rep., 349, 125
Becker G. D., Aloisio A. D.., Christenson H. M., Zhu Y., Worseck G., Bolton J. S., 2021, MNRAS, 508, 1853
Behnel S., Bradshaw R., Citro C., Dalcin L., Seljebotn D. S., Smith K., 2011, Comp. Sci. Eng., 13, 31
Benson A. J., 2012, New Astron., 17, 175
Benson A. J., Cannella C., Cole S., 2016, Comput. Astrophys. Cosmology, 3, 3
Bond J. R., Cole S., Efstathiou G., Kaiser N., 1991, ApJ, 379, 440

$70\,h^{-1}\,{\rm Mpc}$, which are slightly smaller than expected for convergence of the statistics. This may also explain why our ratio $\sigma_{\rm measured}/\sigma_{\rm theoretical}$ sits above unity for the largest scales (i.e. where it is expected to be Gaussian).

Bouwens R. J. et al., 2015, ApJ, 803, 1
Bouwens R. J. et al., 2021, AJ, 162, 47
Bower R. G., 1991, MNRAS, 248, 332
Bowman J. D., Rogers E. E., Monsalve R. A., Mozdzen T. J., Mahesh N., 2018, Nature, 555, 67
Charlot S., Fall S. M., 2000, ApJ, 539, 718
Cole S., Lacey C. G., Baugh C. M., Frenk C. S., 2002, MNRAS, 319, 168
Cora S. A. et al., 2018, MNRAS, 479, 2
Croton D. J. et al., 2016, ApJS, 222, 22
Das A., Mesinger A., Pallottini A., Ferrara A., Wise J. H., 2017, MNRAS, 469, 1166
Davies F. B. et al., 2018, ApJ, 864, 142
Elahi P. J., Cañas R., Poulton R. J., Tobar R. J., Willis J. S., Lagos C. D. P., Power C., Robotham A. S., 2019a, PASA, 36, 1
Elahi P. J., Poulton R. J., Tobar R. J., Cañas R., Lagos C. D. P., Power C., Robotham A. S., 2019b, PASA, 36, 1
Feng Y., Di-Matteo T., Croft R. A., Bird S., Battaglia N., Wilkins S., 2016, MNRAS, 455, 2778
Fialkov A., Cohen A., Barkana R., Silk J., 2017, MNRAS, 464, 3498
Field G. B., 1958, PIRE, 46, 240
Fragos T. et al., 2013, ApJ, 764, 41
Furlanetto S. R., Zaldarriaga M., Hernquist L., 2004, ApJ, 613, 1
Furlanetto S. R., McQuinn M., Hernquist L., 2006a, MNRAS, 365, 115
Furlanetto S. R., Peng Oh S., Briggs F. H., 2006b, Phys. Rep., 433, 181
Geil P. M. et al., 2016, MNRAS, 462, 804
Gnedin N. Y., 2014, ApJ, 793, 29
Gnedin N. Y., Madau P., 2022, Living Rev. Comput. Astrophys., 8, 3
Greig B., Mesinger A., 2015, MNRAS, 449, 4246
Greig B., Mesinger A., 2017, MNRAS, 472, 2651
Greig B., Mesinger A., Davies F. B., Wang F., Yang J., Hennawi J. F., 2022a, MNRAS, 512, 5390
Greig B., Wyithe J. S. B., Murray S. G., Mutch S. J., Trott C. M., 2022b, MNRAS, 516, 5588
Harris C. R. et al., 2020, Nature, 585, 357
Hoag A. et al., 2019, ApJ, 878, 12
Hunter J. D., 2007, Comp. Sci. Eng., 9, 90
Hutter A., Dayal P., Yepes G., Gottlöber S., Legrand L., Ucci G., 2021, MNRAS, 503, 3698
Iliev I. T., Mellema G., Ahn K., Shapiro P. R., Mao Y., Pen U. L., 2014, MNRAS, 439, 725
Jung I. et al., 2020, ApJ, 904, 144
Kannan R., Garaldi E., Smith A., Pakmor R., Springel V., Vogelsberger M., Hernquist L., 2022, MNRAS, 511, 4005
Kauffmann G., 1996, MNRAS, 281, 475
Kaur H. D., Gillet N., Mesinger A., 2020, MNRAS, 495, 2354
Kaurov A. A., Gnedin N. Y., 2015, ApJ, 810, 154
Kim H. S., Wyithe J. S. B., Park J., Poole G. B., Lacey C. G., Baugh C. M., 2016, MNRAS, 455, 4498
Koopmans L. V. et al., 2015, Proc. Sci. The Cosmic Dawn and Epoch of Reionisation with SKA. SISSA, Trieste, PoS#1
Lacey C., Cole S., 1993, MNRAS, 262, 627
Lagos C. d. P., Tobar R. J., Robotham A. S. G., Obreschkow D., Mitchell P. D., Power C., Elahi P. J., 2018, MNRAS, 481, 3573
Maity B., Choudhury R., 2022, MNRAS, 511, 2239
Mason C. A. et al., 2019, MNRAS, 485, 3947
McGreer I. D., Mesinger A., D'Odorico V., 2015, MNRAS, 447, 499
McQuinn M., 2012, MNRAS, 426, 1349
Mertens F. G. et al., 2020, MNRAS, 493, 1662
Mesinger A., 2019, The Cosmic 21-cm Revolution: Charting the first billion years of our Universe. IOP Publishing, Bristol
Mesinger A., Furlanetto S., Cen R., 2011, MNRAS, 411, 955
Mesinger A., Ferrara A., Spiegel D. S., 2013, MNRAS, 431, 621
Mesinger A., Aykutalp A., Vanzella E., Pentericci L., Ferrara A., Dijkstra M., 2015, MNRAS, 446, 566
Mineo S., Gilfanov M., Sunyaev R., 2012, MNRAS, 419, 2095
Mondal R., Bharadwaj S., Majumdar S., Bera A., Acharyya A., 2015, MNRAS, 449, L41
Mondal R., Bharadwaj S., Majumdar S., 2016, MNRAS, 456, 1936
Morales M. F., Wyithe J. S. B., 2010, ARA&A, 48, 127
Murray S., Greig B., Mesinger A., Muñoz J., Qin Y., Park J., Watkinson C., 2020, J. Open Source Softw., 5, 2582
Mutch S. J., Geil P. M., Poole G. B., Angel P. W., Duffy A. R., Mesinger A., Wyithe J. S. B., 2016, MNRAS, 462, 250
Ocvirk P. et al., 2016, MNRAS, 463, 1462
Ocvirk P. et al., 2020, MNRAS, 496, 4087
Pacucci F., Mesinger A., Mineo S., Ferrara A., 2014, MNRAS, 443, 678
Parkinson H., Cole S., Helly J., 2008, MNRAS, 383, 557
Peebles P. J. E., 1980, The large-scale structure of the universe. Princeton Univ. Press, Princeton
Planck Collaboration, A13 2016, A&A, 594
Planck Collaboration VI, 2020, A&A, 641, A6
Pritchard J. R., Furlanetto S. R., 2007, MNRAS, 376, 1680
Pritchard J. R., Loeb A., 2012, Rep. Prog. Phys., 75, 086901
Qin Y. et al., 2017, MNRAS, 472, 2009
Qin Y., Mesinger A., Park J., Greig B., Muñoz J. B., 2020, MNRAS, 495, 123
Qin Y., Mesinger A., Greig B., Park J., 2021, MNRAS, 501, 4748
Qiu Y., Mutch S. J., da Cunha E., Poole G. B., Stuart Wyithe J. B., 2019, MNRAS, 489, 1357
Qiu Y., Mutch S. J., Elahi P. J., Poulton R. J. J., Power C., Wyithe J. S. B., 2020, MNRAS, 500, 493
Rosdahl J. et al., 2018, MNRAS, 479, 994
Santos M. G., Ferramacho L., Silva M. B., Amblard A., Cooray A., 2010, MNRAS, 406, 2421
Schaller M., Gonnet P., Chalk A. B. G., Draper P. W., 2016, PASC '16: Proceedings of the Platform for Advanced Scientific Computing Conference, 1, 1
Seiler J., Hutter A., Sinha M., Croton D., 2019, MNRAS, 487, 5739
Singh S. et al., 2022, Nat. Astron., 6, 607
Sinha M., Garrison L. H., 2020, MNRAS, 491, 3022
Sobacchi E., Mesinger A., 2014, MNRAS, 440, 1662
Somerville R. S., Davé R., 2015, ARA&A, 53, 51
Song M. et al., 2016, ApJ, 825, 5
Songaila A., Cowie L. L., 2010, ApJ, 721, 1448
Springel V. et al., 2018, MNRAS, 475, 676
Stefanon M., Bouwens R. J., Labbé I., Illingworth G. D., Gonzalez V., Oesch P. A., 2021, ApJ, 922, 29
The HERA Collaboration et al., 2022, Improved Constraints on the 21 cm EoR Power Spectrum and the X-Ray Heating of the IGM with HERA Phase I Observations
Tinker J. L., Robertson B. E., Kravtsov A. V., Klypin A., Warren M. S., Yepes G., Gottlöber S., 2010, ApJ, 724, 878
Trott C. M. et al., 2020, MNRAS, 493, 4711
Van Rossum G., Drake F. L., Jr, 1995, Python reference manual. Centrum voor Wiskunde en Informatica, Amsterdam
Ventura E. M., Trinca A., Schneider R., Graziani L., Valiante R., Wyithe J. S. B., 2023, MNRAS
Virtanen P. et al., 2020, Nat. Methods, 17, 261
Visbal E., Bryan G. L., Haiman Z., 2020, ApJ, 897, 95
Wang F. et al., 2020, ApJ, 896, 23
Whitler L. R., Mason C. A., Ren K., Dijkstra M., Mesinger A., Pentericci L., Trenti M., Treu T., 2020, MNRAS, 495, 3602
Wold I. G. B. et al., 2022, ApJ, 927, 36
Wouthuysen S. A., 1952, AJ, 57, 31
Wyithe J. S. B., Loeb A., 2004, Nature, 432, 194

This paper has been typeset from a TEX/LATEX file prepared by the author.